Turbulence and entrainment in an atmospheric pressure dielectric barrier plasma jet

Youssef Morabit, Richard D. Whalley, Eric Robert, Mohammad I. Hasan, James L. Walsh

Plasma Processes and Polymers

Turbulence and entrainment in an atmospheric pressure dielectric barrier plasma jet

Journal:	*Plasma Processes and Polymers*
Manuscript ID	Draft
Wiley - Manuscript type:	Full Paper
Date Submitted by the Author:	n/a
Complete List of Authors:	Morabit, Youssef; University of Liverpool, Department of Electrical Engineering & Electronics Whalley, Richard; Newcastle University, School of Mechanical and Systems Engineering robert, eric; CNRS/Univ Orleans, UMR 6606 GREMI Hasan, Mohammad; University of Liverpool, Department of Electrical Engineering & Electronics Walsh, James; University of Liverpool, Department of Electrical Engineering & Electronics
Keywords:	

Manuscript number DOI:10.1002/ppap.

Article type: Full Paper

Turbulence and entrainment in an atmospheric pressure dielectric barrier plasma jet.

Y. Morabit[1], R. D. Whalley[2], E. Robert[3], M. I. Hasan[1] & J. L. Walsh[1*]

[1] Centre for Plasma Microbiology, Department of Electrical Engineering & Electronics, University of Liverpool, L69 3GJ, UK.

[2] School of Mechanical and Systems Engineering, Newcastle University, NE1 7RU, UK.

[3] GREMI UMR 7344 CNRS/Université d'Orléans, Orléans, 45067, France.

Abstract

Particle Imagining Velocimetry, Laser Induced Fluorescence and computational modeling are used to quantify the impact of plasma generation on air entrainment into a helium plasma jet. It is demonstrated that discharge generation yields a minor increase in the exit velocity of the gas. In contrast, the laminar to turbulent transition point is strongly affected, attributed to an increase in plasma-induced perturbations within the jet shear layer. The temporal decay of laser induced fluorescence from OH is used as an indicator for humid air within the plasma. The results show that plasma-induced perturbations increase the quenching rate of the OH fluorescent state; indicating shear layer instabilities play a major role in determining the physicochemical characteristics of the plasma.

*Corresponding author: jlwalsh@liverpool.ac.uk

1 Introduction

Atmospheric pressure plasma jets have been widely used in many healthcare and materials processing applications, ranging from etching and deposition to microbial decontamination and cancer therapy.[1-5] Perhaps the most widely used plasma jet configuration is based on the dielectric barrier discharge employing a noble gas such as helium or argon; typically, the gas is flushed through a dielectric capillary and subjected to an applied voltage using one or more electrodes placed inside and/or outside of the capillary. On application of a time-varying voltage of sufficient magnitude to cause breakdown, a discharge forms within the capillary and propagates as a fast-moving ionization wave along the noble gas channel, ultimately exiting the capillary and extending into the surrounding quiescent air. From an application perspective, the interaction between the propagating plasma plume and the surrounding air is of great importance as many atmospheric pressure plasma-based applications rely on reactive oxygen and nitrogen species (RONS), many of which are created when the noble gas plasma interacts with the surrounding air.

A large number of studies have considered the impact that plasma generation has on the characteristics of the flowing noble gas. It has been widely reported that the generation of plasma in a buoyant axisymmetric jet configuration leads to a rapid transition from laminar to turbulent flow.[6-9] It is commonly assumed that gas heating and Electrohydrodynamic (EHD) forces play a role in creating turbulence within the flowing gas channel, with the latter being considered as the dominant mechanism. Indeed, Park et al. used a pulsed plasma jet to demonstrate that EHD forces are primarily exerted by space charge drifting in the applied electric field following streamer propagation.[10, 11] Whalley and Walsh demonstrated that the spatially developing velocity fields in an inhomogeneous axisymmetric plasma jet flow are turbulent and self-similar, with characteristics matching the turbulent velocity fields which develop naturally with increasing distance from the jet exit. The study posited that the production of turbulence is related to the small-amplitude plasma-induced body forces causing perturbations in the unstable shear layers at the jet exit, which grow as

they move downstream, creating turbulence.[12, 13] Using an order-of-magnitude analysis, it was predicted that the presence of a discharge should only increase the jet exit velocity by approximately 10%.[8]

To characterize the chemical species produced downstream of the jet orifice, multiple invasive and non-invasive diagnostic techniques have been adopted, including tunable diode laser absorption spectroscopy (TDLAS),[14] mass spectroscopy (MS),[15] Fourier transform infrared spectroscopy (FTIR),[16] Laser-Induced Fluorescence (LIF) and Two-photon Absorption Laser-Induced Fluorescence (TALIF).[17-19] Of all the techniques investigated, LIF based methods are particularly convenient as they provide the high spatiotemporal resolution required to accurately investigate the complex downstream chemistry in a plasma jet while facilitating the quantification of absolute radical densities. Regardless of the diagnostic technique used, it is clear that a significant proportion of the reactive chemical species produced within the downstream region of the jet are a result of reactions between the noble gas plasma and molecular gas impurities entrained from the surrounding environment, which is typically humid air. Given that the interplay between the propagating plasma plume and ambient environment has a considerable impact on the physicochemical properties of the plasma jet and, therefore, on the application efficacy, understanding the underpinning mechanisms of how air becomes entrained within the flowing noble gas channel is of vital importance.

This study investigates the entrainment of air into a helium plasma jet and explores the hypothesis that small perturbations within the jet shear layer resulting from plasma generation not only result in the early onset of turbulence but also act to increase entrainment of air into the laminar region of the jet. Particle imaging velocimetry (PIV) was used to quantify the fluid dynamics of the helium jet flow beyond the jet orifice and combined with LIF to provide a sensitive means of assessing the entrainment of humid air into the discharge.

2 Experimental and computation methods

2.1 Plasma Jet and PIV setup

The plasma jet used in this study comprised of a quartz capillary with an inner diameter D, equal to 3 mm and outer diameter of 5 mm, a metallic strip was wrapped around the outer diameter of the capillary to act as a ground electrode, as shown in **Figure 1**. A tungsten pin was positioned coaxially within the quartz capillary and connected to a high-voltage sinusoidal power operating at a frequency of 20 kHz. Two applied voltage cases were examined in this study, 14 and 10 kVpp, with the latter being just above the point of gas breakdown. Helium gas with a purity of 99.999% flowed through the capillary at 2 Standard Litres per Minute (SLM), giving a maximum exit velocity, U_m, equal to 9.4 m s^{-1}.

To quantify the flow field created by the plasma jet, PIV measurements were undertaken using the experimental setup shown in Figure 1. The plasma jet was inserted into a large sealed chamber (volume > 2 m^3), which was seeded using oil droplets with a nominal size of 1 µm. The chamber ensured that the plasma jet flow was not influenced by any external draughts. A similar experimental arrangement was used in the previous works of the authors,[8] where it was observed that an insufficient number of seeding particles were entrained within the laminar region of the jet to obtain reliable PIV measurements. To overcome this challenge, the helium flow into the jet capillary was seeded using oil droplets, which also had a nominal size of 1 µm. The addition of oil droplets to the helium gas flow has an obvious potential to disrupt the discharge; while such changes are difficult to assess, the breakdown voltage and length of plasma plume were found not to change significantly. Furthermore, Rayleigh scattering was used to obtain an approximate indication of the laminar region length in an un-seeded jet and a close agreement was observed when compared to the PIV measurements on the seeded jet, suggesting the presence of the seeding particles had a minimal impact on the fluid dynamic properties of the system. Given the nominal

size of the seeding particles, the Stokes number was found to be less than 0.1, thus ensuring that the particles followed the fluid flow closely with tracing errors being < 1%.[20]

Planar velocity measurements were conducted using a 2D particle image velocimetry system from TSI inc. The system consisted of a double pulsed Nd:YLF laser operating at 200 Hz with a pulse duration of 100 ns at a wavelength of 527 nm and was used to generate a 1 mm thick light sheet that was projected into the seeding chamber and across the plasma jet orifice. A high-speed Phantom Miro Lab 340 camera was positioned outside the seeding chamber normal to the laser sheet and synchronized with the laser such that each frame captured a single laser pulse. A spatial calibration was performed and the time delay between consecutive laser pulses (Δt) was set to 30 µs, a value chosen to capture the movement of oil droplets over a grid with spatial dimensions of 350 µm^2, enabling the velocity vectors to be computed using a recursive cross-correlation technique. For each measurement condition, the plasma jet was operated for several seconds before data capture to ensure steady-state conditions were achieved. Each dataset comprised of 800 frames that were used to make 400 individual velocity vector maps; in the case of time-averaged measurements, all 400 vector maps were averaged and presented as a single figure.

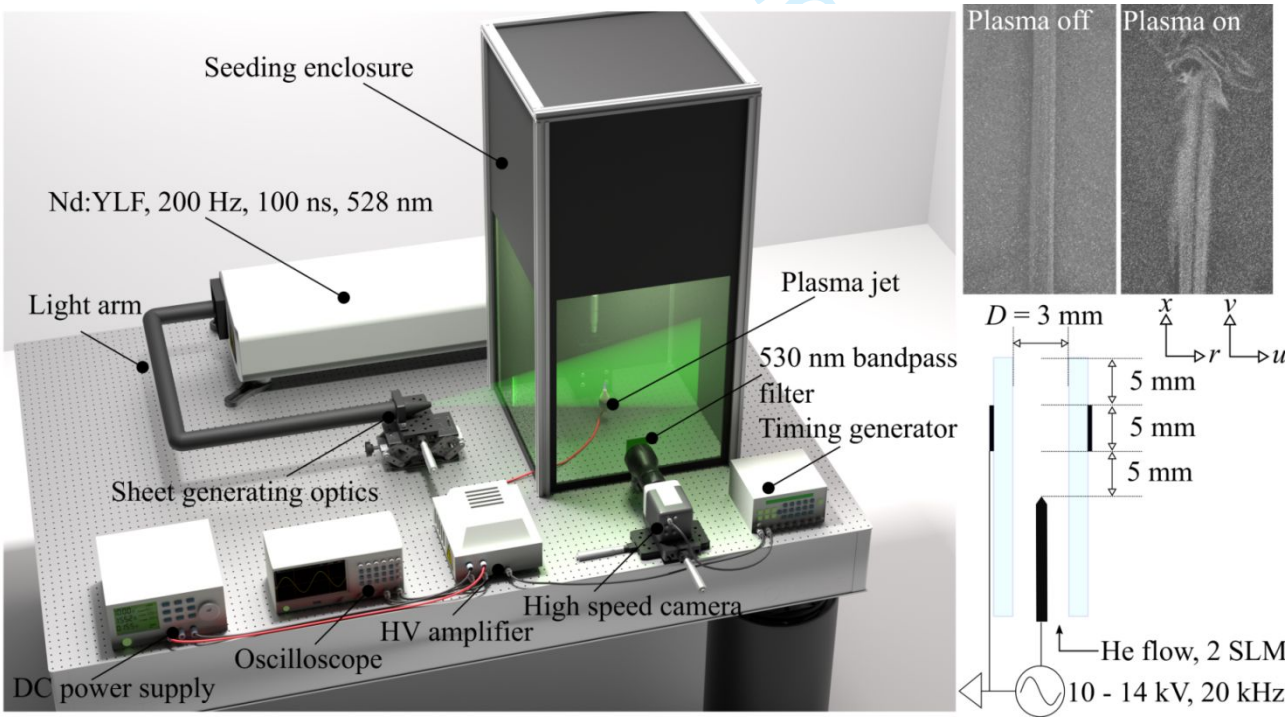

Figure 1. Diagram showing the layout of the particle imaging velocimetry experiment and configuration of the plasma jet device, with representative PIV images for the plasma off and plasma on cases, vectors *v* and *u* represent the axial and radial velocity components, respectively.

2.2 LIF setup and OH density calibration

The LIF measurement system used in the investigation is shown in **Figure 2**, the system was used to measure OH radical density and to obtain an indication of air entrainment within the plasma plume through the measurement of the radiative decay time of the laser-excited OH(A) state. The system comprised of a tunable dye laser (Sirah Cobra Stretch with second harmonic generation unit) pumped by a 6 ns pulsed Nd:YAG laser with a wavelength of 532 nm, pulse energy of 120 mJ and a repetition rate of 10 Hz. The dye laser was tuned to generate an output at a wavelength 282.58 nm to excite the $P_1(2)$ transition from the $f_1(2)$ rotational level of OH X($v'' = 0$) to the $F_1(1)$ rotational level of OH A($v' = 1$). Numerous other studies have used a similar excitation scheme due to the $P_1(2)$ transition being spectrally separated from adjacent lines and the $f_1(2)$ level having the largest relative population in the temperature range under investigation.[21]

The 282.58 nm beam emitted from the dye laser was measured to have a pulse energy in excess of 17 mJ, a value several orders of magnitude above the range linear LIF measurements are typically made (1 – 10 μJ).[22] Operation beyond the linear region greatly complicates the interpretation of the results, as the ground rotational level is significantly depleted by light absorption and partially refilled by fast rotational redistribution, altering the LIF outcome dependent on the unknown gas composition and temperature. To attenuate the laser energy to a suitable range an optical arrangement similar to that employed by Ries et al. was adopted,[17] two quartz plates were angled to split the beam as shown in Figure 2, with a small fraction being reflected towards the plasma jet and the majority of the beam passing through to beam dumps mounted behind each plate. Following attenuation, the beam was directed through an uncoated quartz plano-convex lens with a focal

length of 1 m, and a pinhole of 1 mm was positioned to act as a spatial filter, further attenuating the beam. Using this approach the maximum pulse energy was found to be approximately 15 μJ; small changes to the Q-switch delay of the pump laser were subsequently used to vary the pulse energy between 1 and 15 μJ. Laser power was measured using a Thorlabs PM100D optical power and energy meter equipped with a thermal volume absorber power sensor.

To capture the fluorescence of excited OH molecules, an Andor iStar740 iCCD camera was fitted with a Jenoptik UV 105 mm f/4.5 imaging lens. The camera arrangement was positioned to face the plasma jet perpendicular to the laser beam. For each image recorded, the iCCD camera was configured to accumulatively capture 500 laser pulses, using an optical gate width equal to 8 ns for each exposure. Following the approach of Verreycken et al.,[21] no bandpass filter was used during LIF measurements to avoid the need for additional corrections in the calibration procedure. A consequence of this approach is the potential for interference of the fluorescent signal from other emissions within the plasma and the Rayleigh scattering signal. A background subtraction of the emission captured with the plasma energized and laser de-tuned was used to correct for light emitted by the plasma and any scattered light. To ensure the measurements were conducted within the linear LIF region, the measured LIF intensity was plotted against laser energy and a linear fit applied. It was determined that the linear range was between 1 μJ to 10 μJ, a value in close agreement with several past LIF investigations.[17, 21]

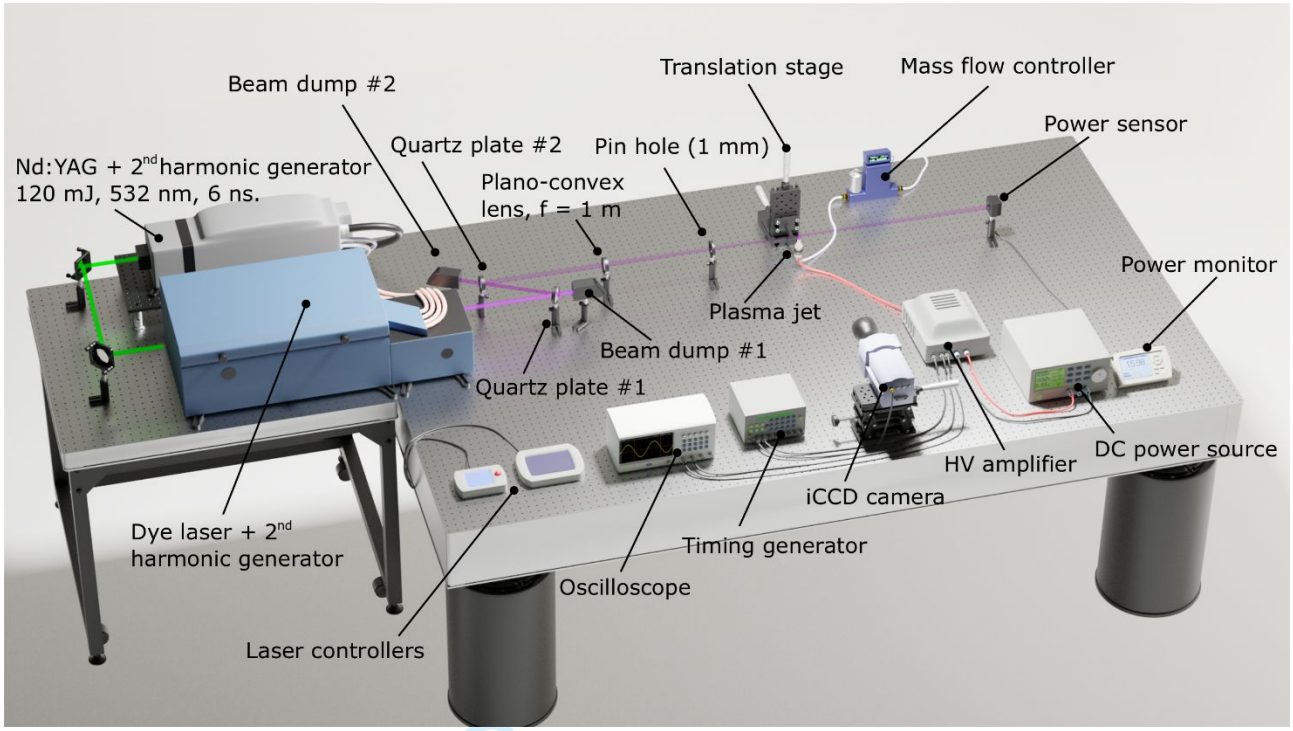

Figure 2. Diagram showing the layout of the Laser-Induced Fluorescence experiment.

Absolute calibration of the LIF signal to determine the density of ground-state OH can be achieved via several methods, including UV absorption, chemical modeling, and Rayleigh scattering.[21, 23] In this investigation, the Rayleigh scattering approach was adopted due to its high degree of accuracy, and a similar methodology to that described by Verreycken et al. was adopted.[21] Calibration by Rayleigh scattering requires detailed knowledge of the rotational and vibrational energy transfer rates, which vary significantly depending on the nature of the quenchers present; thus an accurate appreciation of the gas composition is essential. Careful consideration must be applied in the case of a plasma jet as the gas composition varies as a function of distance from the jet orifice; further details on this are provided in section 2.3. In addition to the gas composition, the gas temperature can also affect the interpretation of the LIF data. To investigate the influence of plasma generation on gas temperature, an Omega FOB100 fiber-optic thermometer was used, the dielectric temperature probe was positioned in the plasma at various points downstream of the jet orifice and the temperature recorded. The temperature was found to vary little with spatial position, with a

maximum of 10 K above ambient located close to the capillary orifice, such observations are in-line with previous studies.[8]

The remainder of the calibration process closely followed that reported previously by Verreycken et al. and will only be summarised in brief here.[21] To obtain Rayleigh scattering data for calibration, the plasma jet was de-energized and supplied with Nitrogen gas at a flow rate of 2 SLM, while not strictly necessary, the nitrogen flow helped to ensure dust from the ambient environment did not enter the measurement region of interest. The laser power was varied from 2 to 15 µJ in 1 µJ increments, and the sum of the Rayleigh scattered signal intensity in a rectangular region of interest measuring 0.36 x 0.36 mm was calculated. The measured Rayleigh scattered signal, S_{Ray} (#counts), can be written as :

$$S_{Ray} = \eta N_n \frac{\partial^{\beta=0}\sigma_0}{\partial\Omega} V_{Ray} I_L t_L \qquad (1)$$

Where η is the calibration constant (#counts sr J^{-1}), N_n is the density of scattering particles (m^{-3}), $\partial^{\beta=0}\sigma_0 / \partial\Omega$ is the differential cross-section for Rayleigh scattering ($m^2\ sr^{-1}$), V_{Ray} is the volume from which Rayleigh scattering is collected (m^3), I_L is the laser irradiance (W m^{-2}) and t_L is the temporal length of the laser pulse (s), which was measured by replacing the power meter shown in Figure 2 with a fast photodetector. After taking into account the non-uniformity of the laser energy density, Equation (1) becomes:

$$S_{Ray} = \eta N_n \frac{\partial^{\beta=0}\sigma_0}{\partial\Omega} E_L \Delta x \quad (2)$$

Where E_L is the laser energy (J), and Δx is the length of the detection volume (m). Following this, the calibration constant η was obtained from the slope α, of the measured Rayleigh intensity as a function of laser energy multiplied by pressure:

$$\eta = \alpha k_B T \frac{\partial^{\beta=0}\sigma_0}{\partial\Omega}\Delta x \qquad (3)$$

Using the calibration factor, the intensity of the laser-induced fluorescence S_{LIF}, can be expressed as:

$$S_{LIF} = \frac{1}{4\pi}\int \eta E n_{exc}(x,y,z,t) A \, dxdydzdt \quad (4)$$

Where E is the energy gap according to the chosen transition, A is the Einstein emission coefficient (s^{-1}), and n_{exc} *(x, y, z, t)* is the density of OH in the excited state. To determine the ground state OH density based on n_{exc} in Equation (4), the 4-level collisional radiative model reported Verreycken et al. was utilized.[21] The model accounted for the variation in gas composition beyond the jet orifice, as described in the following section.

2.3 Computational model and statistical analysis methodology

To account for the varying composition of gas downstream of the jet orifice, a computational model was developed that solved for the velocity field of the gas mixture in addition to the mass fractions of its constituents, namely N_2, O_2, H_2O, and He. To obtain the velocity field, the model solved the mass continuity Equation (5) and the momentum conservation Equation (6). To compute the gas composition, the mass continuity equation, given by Equation (7), was solved for three species, while the mass fraction of the fourth was determined from the pressure constraint. All equations were solved in steady-state mode (*i.e.,* time-independent equations) :

$$\nabla \cdot \left(\rho \vec{u}\right) = 0 \qquad (5)$$

$$\rho\left(\vec{u}\cdot\nabla\right)\vec{u} = -\nabla p + \nabla\cdot\left(\mu\left(\nabla\vec{u} + \nabla\vec{u}^{T}\right) - \frac{2}{3}\mu\left(\nabla\cdot\vec{u}\right)I\right) - \left(\rho-\rho_0\right)g \qquad (6)$$

$$\rho\left(\vec{u}\cdot\nabla\right)\omega_i + \nabla\cdot\left(\vec{\Gamma}_i\right) = 0 \qquad (7)$$

Where ρ is the density of the gas mixture (kg m^{-3}), $\vec{u}$ is the velocity field of the gas mixture (m s^{-1}), p is the gas mixture's pressure (Pa), μ is the gas mixture's viscosity (Pa s), I is the identity matrix, ρ_0 is the density of air (kg m^{-3}), and g is the gravitational constant (m s^{-2}), ω_i is the mass fraction of the i^{th} species, and Γ_i is the diffusive flux of the i^{th} species, which is calculated according to Maxwell-Stefan theory for diffusion as given by Equation (8-10).[24, 25]

$$\vec{\Gamma}_i = \rho\omega_i\vec{V}_i \tag{8}$$

$$\nabla x_i = \sum_{j=1}^{4}\frac{x_i x_j}{D_{ij}}\left(\vec{V}_j - \vec{V}_i\right) + \frac{\nabla p}{p}\left(\omega_i - x_i\right) \tag{9}$$

$$x_i = \frac{M_n}{M_i}\omega_i \tag{10}$$

Where $\vec{V}_i$ is the diffusion velocity of the i^{th} species (m s^{-1}), x_i is the mole fraction of the i^{th} species (dimensionless), which is related to the mass fraction by Equation (8), and D_{ij} is the binary diffusion coefficients between the i^{th} and the j^{th} species (m^2 s^{-1}). A list of the binary diffusion coefficients used in the model is given in Table 1. It should be noted that Equation (9) is incorporated in the model as a constraint linking the flux term and the mass fraction term in Equation (7). In Equation (10), M_i and M_n are the molecular weight of the i^{th} species and the average molecular weight, respectively (kg mol^{-1}). Lastly, the computational domain and the boundary conditions used are described in the appendix.

Table 1. A list of binary diffusion coefficients used in the model.

Combination	Diffusion coefficient [m^2 s^{-1}]	Reference
$N_2 - He$	6.78×10^{-5}	[26]
$N_2 - O_2$	2.09×10^{-5}	[27]
$N_2 - H_2O$	2.54×10^{-5}	[28]
$O_2 - He$	7.36×10^{-5}	[26]
$He - H_2O$	8.36×10^{-5}	[28]
$O_2 - H_2O$	3.185×10^{-5}	[28]

As stated in the introduction section, it is hypothesized that plasma-induced turbulence affects the flow's velocity field and thus the gas composition. To account for such effects in the computational model, the Reynolds-Averaged Navier-Stokes (RANS) approach for modeling turbulence was followed, where a turbulent viscosity μ_T (also known as eddy viscosity) was added to the viscosity of the gas mixture. The eddy viscosity is a mathematical means to describe the loss of momentum of the flow as a result of turbulence as an "effective" viscosity that is added to the physical viscosity of the fluid. Similarly, a turbulent diffusivity D_T is added to the binary diffusion coefficients.[29] The computation of the eddy viscosity is typically done using one of the conventional RANS turbulence models, such as the $k-\varepsilon$ model. Considering that such models were calibrated for flows without plasma, their use for plasma modified flows will yield results with unknown accuracy. To overcome this challenge, statistical analysis of the PIV data was conducted to obtain the necessary parameters to calculate the eddy viscosity resulting from the plasma generation. Following the $k-\varepsilon$ modeling approach, the turbulent kinetic energy k ($m^2\ s^{-2}$) and the turbulent kinetic energy dissipation rate ε ($m^2\ s^{-3}$) are defined by Equation (11) and (12).[29]

$$k = \frac{1}{2}\left(\overline{u'^2} + \overline{v'^2}\right) \tag{11}$$

$$\varepsilon = 2\nu\overline{s'_{ij} \cdot s'_{ij}} \tag{12}$$

Where u' and v' are the time fluctuating velocity field components with respect to the average velocity field, which were calculated from PIV data by subtracting the time-averaged velocity field from each of the 400 instantaneous velocity maps captured during a measurement, then averaging the square of these fluctuations. In Equation (12), ν is the kinematic viscosity ($m^2\ s^{-1}$), and s'_{ij} is the fluctuating deformation rate of the fluid (s^{-1}), which was calculated from the PIV data as outlined by Xu and colleagues.[30] After calculating k and ε the eddy viscosity was calculated according to Equation (13).[29]

$$\mu_T = \rho C \frac{k^2}{\varepsilon} \tag{13}$$

Where C is a constant equal to 0.0016 and ρ is the self-consistent gas mixture density calculated by the model. The turbulent diffusivity D_T is related to the eddy viscosity by Equation (14).[25]

$$D_T = \frac{\mu_T}{\rho Sc_T} \tag{14}$$

Where Sc_T is the turbulent Schmidt number, obtaining an accurate value for this in a plasma-modified flow is not possible; however, the turbulent Schmidt number is close to unity for a wide variety of gas flows under very diverse conditions; hence it is assumed to be 1 in this investigation.[31] The model is subsequently solved with the experimental input of μ_T and D_T, which were smoothed and mirrored, then added to their physical counterpart quantities. The model was solved for both applied voltage cases investigated in this work, in addition to an unperturbed laminar case, where the eddy viscosity and diffusivity were set to zero.

The radiative collisional model consisted of a system of Ordinary Differential Equations (ODE) describing the LIF transitions. The system was solved at every point in the computational domain close to the jet's orifice (x< 20 mm, x/D < 7), with the gas composition required for the ODEs being taken from that calculated by the fluid flow model. To quantify the density of ground-state OH, the 4-level model reported by Verreycken et al. was adopted.[21] The experimental parameters used in this study are summarised in Table 2. To validate the developed computational model, the predicted LIF signal decay times were compared to those measured experimentally at multiple points along the jet axis; a close agreement was observed and is further discussed in the results section.

Table 2. Experimental parameters used in LIF measurements and absolute density calibration

Parameter	Description	Value
λ_L	Laser wavelength	282.58 [nm]
$\Delta\lambda_L$	Linewidth of the laser	0.95 [pm]
g_{int}	Overlap integral	0.017 [m]
A_L	Area of the laser beam	0.0746 [mm^2]
E_L	Laser energy per pulse	10 [μJ]
τ_L	Temporal FWHM of the laser pulse	6 [ns]
Δx	Length of the detection volume	0.359 [mm]
Δy	Width of the detection volume	0.359 [mm]
Δs	The spatial FWHM of the laser beam at the observation point	0.1795 [mm]

3 Results and discussion

3.1 Influence of plasma on jet velocity and turbulence generation

PIV measurements were undertaken to quantify the velocity of the flowing helium gas and the resulting perturbation of the surrounding quiescent air beyond the jet orifice. **Figure 3** (a-c) shows the ensemble-averaged two-component velocity vector maps and velocity magnitude (U) normalized to the measured exit velocity (U_m) for the 0 kV, 10 kV, and 14 kV cases, respectively. Without a plasma discharge (0 kV case), the undisturbed helium flow appeared laminar over the entire measurement region, confirmed by the ensemble-averaged centreline velocity (U_c) profile in Figure 3(d). On the application of a 10 kV sinusoidal waveform, a weak discharge was observed to form, indicating gas breakdown had been achieved; under such conditions, little obvious change to the velocity profile was observed. An increase in applied voltage from 10 kV to 14 kV led to an increase in the length of the visible plasma plume. Comparing Figure 3(b) and 3(c) highlights the impact of the applied voltage on the flow structure downstream of the jet orifice, with the higher applied voltage resulting in a significant reduction in the length of the laminar flow region. From the ensemble-averaged centreline velocity, an abrupt change in gradient is observed at approximately 8 x/D, indicating a transition to turbulence. While such results are perhaps the first

quantitative measurements of velocity within a plasma jet, they remain highly consistent with previous observations made using qualitative methods such as Schlieren imaging.[9, 32]

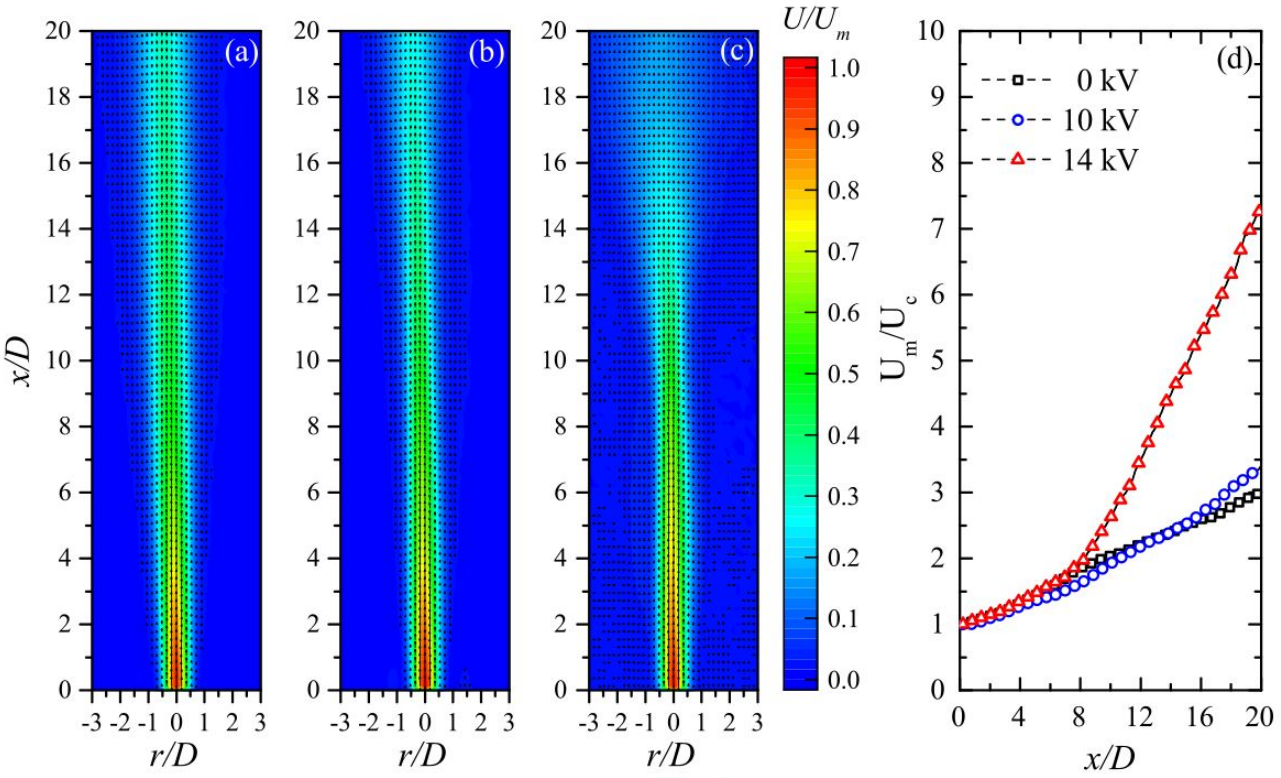

Figure 3. Ensemble averaged particle imaging velocimetry measurements of the plasma jet obtained at applied voltages of (a) 0 kV, (b) 10 kV, and (c) 14 kV, (d) shows the ensemble-averaged centreline velocity (U_c) normalized to the measured exit velocity (U_m).

In absolute terms, the generation of plasma with an applied voltage of 14 kV was found to increase U_m by 0.94 m s^{-1}, representing a relatively modest increase of approximately 10% compared to the 0 kV case. Such increases in velocity are in line with those predicted by others and are a consequence of gas heating and electrohydrodynamic forces induced by the plasma, with the latter mechanism being the most likely dominant factor.[8, 10] Notably, the modest change in velocity associated with plasma generation cannot directly explain the rapid transition to turbulence observed when comparing Figure 3(a) and 3(c). Past studies on turbulence generation in axisymmetric round jets have revealed that turbulence initiates due to instabilities within the shear layers at the jet exit that

become amplified as they travel downstream.[33-36] As the instabilities grow, they cause velocity fluctuations, Reynolds shear stresses, and thus the production of turbulence.[8] Many previous studies have explored 'excited' jets that employ alternative means to perturb the jet flow in order to investigate the mechanisms of turbulence generation.[37-42] For example, the impact of sonic excitation on the jet velocity profile shows a remarkable similarity to those observed in this study[38]; hence it is posited that plasma generation is an alternative means to excite an axisymmetric round jet, resulting in the rapid onset of turbulence through increased shear layer instability with little change to velocity.

While the growth of small-scale instabilities within the jet shear layer has a significant impact on the laminar to turbulent transition, they also provide a mechanism to enhance entrainment of quiescent air into the laminar region of the plasma jet.[42] To investigate the influence of plasma generation on instabilities in the jet shear layer, the eddy viscosity μ_T was calculated. The eddy viscosity profiles for the two plasma cases investigated in this work are shown in **Figure 4** (a-b). Three characteristic zones can be observed within the profiles, the first is close to the jet orifice, where a region of low μ_T exists, which can be explained by the fact that this is the laminar region where the amplitude of velocity fluctuations is small, leading to low turbulent kinetic energy k, and consequently, a low μ_T as Equation (13) shows. The second zone (e.g., 4 – 10 x/D in Figure 4(b)) coincides with the transition region, as inferred from Figure 3(d), where the value of μ_T peaks. This is attributed to the large scale fluctuations/eddies starting to appear in the transition region, leading to high turbulent kinetic energy k, considering that such large fluctuations live long enough to be transported downstream, the dissipation rate of the turbulent energy ε is relatively low in this region, thus leading to a peak of μ_T as follows from Equation (13). The third zone (e.g. > 10 x/D in Figure 4(b)) coincides with the turbulent region, as inferred from Figure 3(d), which has a moderate value of μ_T. As known from the energy cascade theory of turbulence,[43] the large eddies generated in the transition region break into smaller eddies in the fully turbulent region, the small eddies are

dissipated into heat due to the physical viscosity of the fluid.[43] In this sense, the turbulent kinetic energy k is high, while the turbulent dissipation rate ε is also high, leading to a moderate value of μ_T. From Figure 4(a-b), it is clear that the eddy viscosity for the 14 kV case has a larger magnitude compared to the 10 kV case, which is consistent with the PIV results presented in Figure 3(b-c). When comparing the average value of μ_T in zone one (x/D < 4) for both cases it is found that μ_T for the 10 kV case is approximately 70%-80% of that for the 14 kV case, indicating that the plasma's perturbation to the flow in the laminar region is more significant for the 14 kV case in comparison to the 10 kV case.

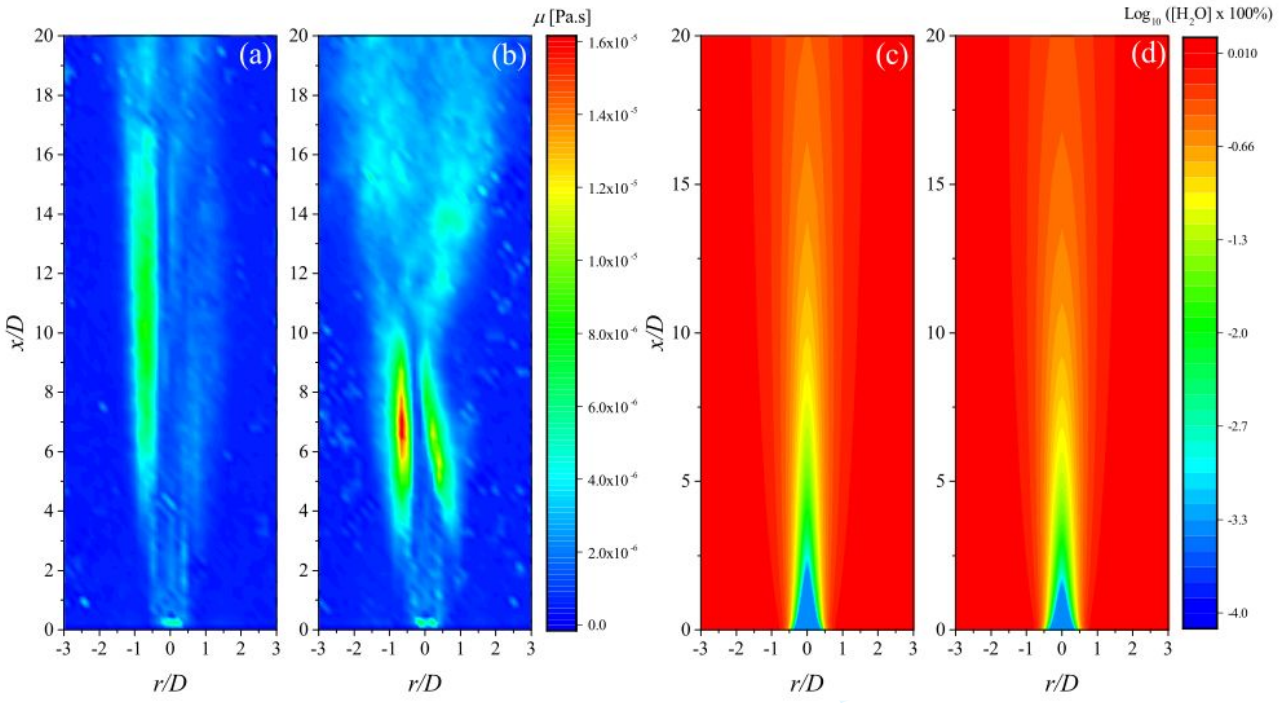

Figure 4. Eddy viscosity calculated from PIV measurements for the (a) 10 kV and (b) 14 kV excited plasma jet and the calculated entrainment of H_2O into the helium flow under (c) 0 kV and (d) 14 kV conditions.

As described in section 2.3, a higher value of the eddy viscosity of μ_T indicates a higher value of eddy diffusivity D_T, which adds to the physical diffusion coefficients, leading to increased entrainment of air into the helium jet for higher values of μ_T. To highlight the impact of the plasma-induced entrainment, Figure 4 (c) and (d) show the computed percentage of H_2O in the gas mixture

for the 0 kV and 14 kV cases, respectively. Notably, the 0 kV case represents an unperturbed laminar flow where quiescent air is entrained due to the physical diffusion only. While in the case of the perturbed flow shown in Figure 4(d), air entrainment occurs due to physical diffusion plus the "effective" eddy diffusion due to turbulence. The centreline concentration of H_2O at the jet exit in both cases was set to 0.00004%, a value obtained from the helium gas provider. Moving downstream to 2 x/D, the level of H_2O in the unperturbed 0 kV case was found to increase to be approximately 0.0005 %. In contrast, the H_2O concentration in the perturbed case was found to be 0.0034 %, representing a 7-fold increase. Further downstream at 6 x/D, the H_2O concentration in the unperturbed case was found to be 0.046%, compared to 0.082% in the perturbed case, representing a 1.8-fold increase. When moving downstream, the difference between the unperturbed case and the 14 kV perturbed case diminishes as a result of the increasing density of the gas mixture, which lowers the value of the eddy diffusivity as defined by Equation (4).

3.2 OH fluorescence decay rate and absolute density

As described by Yonemori et al. the decay rate of the LIF signal from OH provides a sensitive indication of the helium-air mixing ratio as the quenching rate of the laser-excited state is strongly influenced by the density of quenching species present within the flowing helium gas (e.g., N_2, O_2, H_2O).[44] In this study, a comparison between the measured LIF decay rate and computed decay rate by the model was used to validate the adopted computational approach describing plasma-induced entrainment, thus enabling the accurate quantification of absolute OH density downstream of the jet exit. **Figure 5** shows the measured and computed LIF decay time as a function of downstream spatial position for both the 10 kV and 14 kV cases; additionally, the predicted decay time for a hypothetical unperturbed (laminar) helium flow is shown. The LIF decay time is shorter at all spatial positions under both 10 and 14 kV excitation compared to what would be observed under idealized laminar conditions. As highlighted in Figure 4 (c) and (d), plasma generation increases air entrainment, which acts to increase the density of quenchers and thus increase the quenching rate of

the OH fluorescent state. This result provides experimental evidence supporting the hypothesis that plasma generation increases the entrainment of air within the helium jet at all spatial positions. The calculated decay times closely match the measured data points, with both cases showing very good agreement.

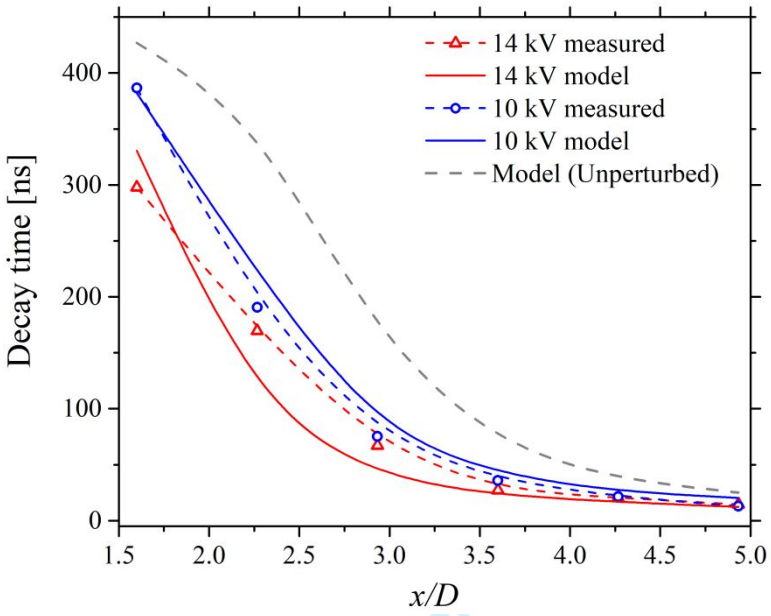

Figure 5. Comparison between measured and calculated decay time of the laser-induced fluorescent signal as a function of downstream distance from the jet orifice.

Using the experimental procedure outlined in section 2.2, the 2D LIF emission profile was compiled for both the 10 kV and 14 kV case and is shown in **Figure 6**(a) and 6(b), respectively. By comparing the centreline LIF intensity obtained from the 2D profile and the computed LIF intensity from the collisional radiative model, the absolute ground state OH density was calculated as a function of downstream position from the jet exit, shown in Figure 6(c). Consistent with the observations made in many previous studies, an increase in applied voltage was observed to increase the peak OH density within the plasma plume.[23] Given that hydrogen-based species densities increase when the air/water vapor fraction increases,[45] it becomes likely that an increase in the applied voltage results in an increase in OH density as a result of not only more intense discharge conditions but also increased entrainment of air and H_2O. Critically, the position of peak

OH density was found to vary depending on the applied voltage. This phenomenon is attributed to the interplay between the physical properties of the plasma (i.e., n_e and T_e) and the fluid dynamics of the helium jet. With an applied voltage of 14 kV, perturbations within the jet shear layer caused by plasma generation induce an early transition to a turbulent flow regime, as confirmed in Figure 3 and 4. Under such conditions, the generation of OH close to the jet exit is locally enhanced due to enhanced H_2O entrainment combined with the relatively intense discharge conditions. Beyond the local maxima, the elevated air mole fraction as a result of the induced turbulence acts to quench the discharge and thus impedes OH generation. Conversely, at the lower applied voltage of 10 kV the discharge is comparatively less intense, meaning less air entrainment and a weaker plasma is formed, both factors contributing to limit OH production. However, less shear layer perturbation causes less air entrainment into the helium flow; thus, the discharge can propagate further from the orifice. Consequently, the concentration of ground-state OH is significantly higher far downstream from the jet exit in the 10 kV case compared to the 14 kV case.

The presented findings have considerable implications from a practical perspective as it has been demonstrated that the density of OH at a given downstream position is strongly influenced by both the discharge characteristics and its interaction with the quiescent background gas. While it is generally assumed that a higher plasma generation voltage results in enhanced production of OH, Figure 6 clearly shows that this only holds true close to the jet orifice. With increasing voltage comes increasing entrainment, which ultimately begins to quench the discharge and negatively affects downstream OH production. Counterintuitively, Figure 6(c) indicates that at a position of 5.3 x/D (i.e., 16 mm from the jet exit), there is an order of magnitude more OH from a plasma generated using 10 kV compared to one generated using 14 kV excitation. These findings demonstrate that the complex interplay between the physicochemical properties of the plasma and the fluid dynamic properties of the flowing noble gas must be carefully considered when designing plasma jet sources for use in applications such as biomedicine and materials processing.

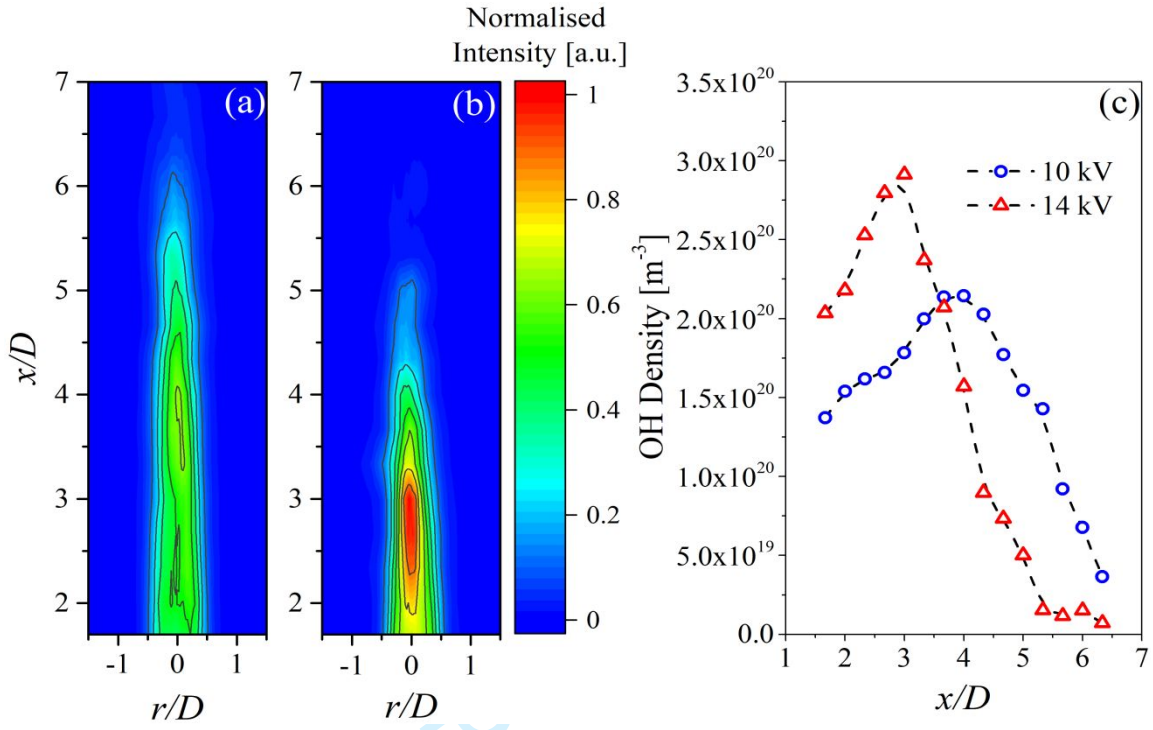

Figure 6. Composite 2D normalised LIF intensity for (a) 10 kV, and (b) 14 kV case. Absolute centreline OH density for the 10 kV and 14 kV case as a function of distance from the jet orifice.

4 Conclusion

This contribution has employed Particle Imaging Velocimetry, Laser-Induced Fluorescence, and Computational Fluid Dynamics to explore the interplay between the propagating plasma plume and the quiescent background air in an axisymmetric dielectric barrier discharge jet. Despite the rapid onset of turbulence observed following plasma ignition, it was demonstrated that the presence of the plasma had little impact on the jet exit velocity of the helium flow. Through statistical analysis of the measured velocity field from the plasma jet under varying excitation conditions, it was determined that plasma generation resulted in shear layer perturbations that grow downstream to initiate the early onset of turbulence.

Using the experimentally derived eddy viscosity, a computational model was developed to calculate the density of humid air entrained within the helium jet flow. To validate the model, the calculated

decay time of the laser-induced fluorescent state of OH was compared against those measured experimentally and found to be in good agreement. Finally, the computational model was used to convert the measured LIF intensity into an absolute OH density from which it was concluded that OH production is strongly influenced by the interplay between the propagating plasma and the background air. At high applied voltages, it was found that OH density increases close to the exit but is rapidly reduced downstream as a result of the elevated air content quenching the discharge.

In summary, this study demonstrates an intricate link between the physicochemical properties of the plasma and its interaction with the quiescent air. As many applications rely on the presence of reactive oxygen and nitrogen species, which are predominantly formed when the plasma interacts with the background environment, the results of this study provide valuable insight into the underpinning mechanisms governing these interactions.

Acknowledgments: JLW & MIH would like to acknowledge the support of the Engineering and Physical Sciences Research Council (Projects EP/S025790/1, EP/S017623/1, EP/R041849/1, and EP/N021347/1). RDW would like to acknowledge the support of the NATO AVT-254 plasma flow control group.

Keywords: LIF; PIV; plasma; turbulence.

[1] A. J. Knoll, P. Luan, A. Pranda, R. L. Bruce, G. S. Oehrlein, *Plasma Process Polym*. **2018**, *15*, 1700217. doi.org/10.1002/ppap.201700217

[2] X. Deng, A. Yu Nikiforov, T. Coenve, P. Cools, G. Aziz, R. Morent, N. De Geyter, C. Leys, *Sci. Rep*., **2015**, *5,* 10138. doi.org/10.1038/srep10138

[3] P. B. Flynn, S. Higginbotham, N. H. Alshraiedeh, S. P. Gorman, W. G. Graham, B. F. Gilmore, *Int. J. Antimicrob. Agents,* **2015**, *46*, 1. doi.org/10.1016/j.ijantimicag.2015.02.026

[4] H. Tanaka, , M. Mizuno, K. Ishikawa, S. Toyokuni, H. Kajiyama, F. Kikkawa, M. Hori, *Plasma*, **2018**, *1*, 1. doi.org/10.3390/plasma1010014

[5] S. Bekeschus, P. Favia, E. Robert, T. Von Woedtke, *Plasma Process Polym.,* **2019**, *16,* 1800033. doi.org/10.1002/ppap.201800033

[6] S. Iseni, A. Schmidt-Bleker, J. Winter, K-D. Weltmann, S. Reuter, *J. Phys. D. Appl. Phys.,* **2014**, *47*, 152001. doi.org/10.1088/0022-3727/47/15/152001

[7] T. Darny, J. M. Pouvesle, J. Fontane, L. Joly, S. Dozias, E. Robert, *Plasma Sources Sci. Technol.,* **2017**, *26*, 105001. doi.org/10.1088/1361-6595/aa8877

[8] R. D. Whalley, J. L. Walsh, *Sci. Rep.,* **2016**, *6,* 31756. DOI:10.1038/srep31756

[9] R. Xiong, Q. Xiong, A. Yu Nikiforov, P. Vanraes, C. Leys, *J. Appl. Phys.,* **2012**, *112*, 033305. DOI:10.1063/1.4746700

[10] S. Park, U. Cvelbar, W. Choe, S. Y. Moon, *Nat. Commun.,* **2018**, *9*, 371. DOI:10.1038/s41467-017-02766-9

[11] M. I.Hasan, J. W. Bradley, *J. Phys. D: Appl. Phys.,* **2016**, *49*, 055203. DOI:10.1088/0022-3727/49/5/055203

[12] M. Boselli, V. Colombo, E. Ghedini, M. Gherardi, R. Laurita, *Plasma Chem. Plasma Process.,* **2014**, *34*, 853. DOI:10.1007/s11090-014-9537-1

[13] A. Michalke, *Journal of Fluid Mechanics*, **1965**, *23*, 3. DOI:10.1017/S0022112065001520

[14] A. V. Pipa, T. Bindemann, R. Foest, E. Kindel, J. Röpcke, K-D. Weltmann, *J. Phys. D. Appl. Phys.,* **2008**, *41*, 194011. DOI:10.1088/0022-3727/41/19/194011

[15] K. McKay, J. S. Oh, J. L. Walsh, J. W. Bradley, *J. Phys. D. Appl. Phys.,* **2013**, *46*, 464018. DOI:10.1088/0022-3727/46/46/464018

[16] A. Schmidt-Bleker, J. Winter, S. Iseni, M. Dünnbier, K-D. Weltmann, S. Reuter, *J. Phys. D. Appl. Phys*., **2014**, *47*, 145201. DOI:10.1088/0022-3727/47/14/145201

[17] D. Riès, G. Dilecce, E. Robert, P. F. Ambrico, S. Dozias, J. M. Pouvesle, *J. Phys. D. Appl. Phys.,* **2014**, *47*, 275401. DOI:10.1088/0022-3727/47/27/275401

[18] S. Reuter, J. Winter, A. Schmidt-Bleker, D. Schroeder, H. Lange, N. Knake, V. Schulz-Von Der Gathen, K. D. Weltmann, *Plasma Sources Sci. Technol.,* **2012**, *21*, 024005. DOI:10.1088/0963-0252/21/2/024005

[19] A. Nikiforov, L. Li, N. Britun, R. Snyders, P. Vanraes, C. Leys, *Plasma Sources Sci. Technol.*, **2014**, *23*, 015015. DOI:10.1088/0963-0252/23/1/015015

[20] C. Tropea, A. L. Yarin, J. F. Foss, *Springer Handbook of experimental fluid mechanics*, Springer, NY, USA **2007**.

[21] T. Verreycken, R. M. Van Der Horst, N. Sadeghi, P. J. Bruggeman, *J. Phys. D. Appl. Phys.,* **2013**, *46*, 464004. DOI:10.1088/0022-3727/46/46/464004

[22] G. Dilecce, L. M. Martini, P. Tosi, M. Scotoni, S. De Benedictis, *Plasma Sources Sci. Technol.,* **2015**, *24*, 034007. DOI:10.1088/0963-0252/24/3/034007

[23] YF. Yue, XK. Pei, XP. Lu, *IEEE Trans. Radiat. Plasma Med. Sci.,* **2017**, *1*, 6. DOI: 10.1109/TRPMS.2017.2757037

[24] R. J. Kee, M. E. Coltrin, P. Glarborg, *Chemically reacting flow: theory and practice*, Wiley-Interscience, Hoboken, NJ, USA **2003**. DOI:10.1002/0471461296

[25] R. B. Bird, W. E. Stewart, E. N. Lightfoot, *Transport Phenomena*, 2nd edition, John Wiley & Sons, NY, USA **2002**.

[26] S. P. Wasik, K. E. McCulloh, *J. Res. Natl. Bur. Stand.,* **1968**, *73A*, 2.

[27] J. Rohling, J. Shen, C. Wang, J. Zhou, C. E. Gu, *Appl. Phys. B*, **2007**, *87*, 355. DOI:10.1007/s00340-007-2595-9

519 [28] C. V. Paganelli, F. K. Kurata, *Respiration Physiology*, **1977**, *30*, 15. DOI:10.1016/0034-
520 5687(77)90018-4
521 [29] T. J. Chung, *Computational fluid dynamics*, Cambridge University Press, Cambridge, UK
522 **2002**.
523 [30] D. Xu, J. Chen, *Exp. Therm. Fluid Sci.,* **2013**, *44* 662.
524 DOI:10.1016/j.expthermflusci.2012.09.006
525 [31] C. Gualtieri, A. Angeloudis, F. Bombardelli, S. Jha, T. Stoesser, *Fluids*, **2017**, *2*, 17.
526 DOI:10.3390/fluids2020017
527 [32] M. Boselli, V. Colombo, M. Gherardi, R. Laurita, A. Liguori, P. Sanibondi, E. Simoncelli, A.
528 Stancampiano, *IEEE Trans. Plasma Sci.,* **2015**, *43*, 3. DOI: 10.1109/TPS.2014.2381854
529 [33] M. Lessen, *Nat. Adv. Comm. Aero., Wash.,* **1950**, *979*.
530 [34] A. Michalke, *J. Fluid Mech.,* **1965**, *23*, 3. DOI:10.1017/S0022112065001520
531 [35] A. Michalke, R. Wille, *Proc. 11th Intern. Congr. Appl. Mech.,* **1965**.
532 [36] A. Michalke, *Prog. Aerosp. Sci.,* **1972**, *12*, 213. DOI:10.1016/0376-0421(72)90005-X
533 [37] H. Sato, *J. Phys. Soc. Jpn.,* **1956**, *11*, 702. DOI:10.1143/JPSJ.11.702
534 [38] H. Sato, *J. Phys. Soc. Jpn.,* **1959**, *14*, 1797. DOI:10.1143/JPSJ.14.1797
535 [39] E. Gutmark, C-M. Ho, *Phys. Fluids*, **1983**, *26*, 2932. DOI:10.1063/1.864058
536 [40] J. Cohen, I. Wygnanski, *J. Fluid Mech*., **1987**, *176*, 191. DOI;10.1017/S0022112087000624
537 [41] S. W. Rienstra, *J. Sound Vib.,* **1983**, *86*, 4. DOI:10.1016/0022-460X(83)91019-2
538 [42] J. Westerweel, C. Fukushima, J.M. Pederson, J. C. R. Hunt, Phys. Rev. Lett.., **2005**, *95*,
539 174501. DOI:10.1103/PhysRevLett.95.174501
540 [43] B. Lautrup, *Physics of continuous matter: exotic and everyday phenomena in the macroscopic*
541 *world*, Institute of Physics, Bristol, UK **2005**.
542 [44] S. Yonemori, Y. Nakagawa, R. Ono, T. Oda, *J. Phys. D. Appl. Phys.,* **2012**, *45*, 225202.
543 DOI:10.1088/0022-3727/45/22/225202

544 [45]T. Murakami, K. Niemi, T. Gans, D. O'Connell, W. G. Graham, *Plasma Sources Sci. Technol.,*

545 **2013**, *22*, 015003. DOI:10.1088/0963-0252/22/1/015003